INTERNATIONAL JOURNAL FOR NUMERICAL METHODS IN FLUIDS
Int. J. Numer. Meth. Fluids 2008; **57**:1577–1602
Published online 5 December 2007 in Wiley InterScience (www.interscience.wiley.com). DOI: 10.1002/fld.1682

Numerical simulation of viscous flow interaction with an elastic membrane

Lisa A. Matthews, Deborah M. Greaves*,† and Chris J. K. Williams

Department of Architecture & Civil Engineering, University of Bath, Bath BA2 7AY, U.K.

SUMMARY

A numerical fluid–structure interaction model is developed for the analysis of viscous flow over elastic membrane structures. The Navier–Stokes equations are discretized on a moving body-fitted unstructured triangular grid using the finite volume method, taking into account grid non-orthogonality, and implementing the SIMPLE algorithm for pressure solution, power law implicit differencing and Rhie–Chow explicit mass flux interpolations. The membrane is discretized as a set of links that coincide with a subset of the fluid mesh edges. A new model is introduced to distribute local and global elastic effects to aid stability of the structure model and damping effects are also included. A pseudo-structural approach using a balance of mesh edge spring tensions and cell internal pressures controls the motion of fluid mesh nodes based on the displacements of the membrane.

Following initial validation, the model is applied to the case of a two-dimensional membrane pinned at both ends at an angle of attack of 4° to the oncoming flow, at a Reynolds number based on the chord length of 4×10^3. A series of tests on membranes of different elastic stiffness investigates their unsteady movements over time. The membranes of higher elastic stiffness adopt a stable equilibrium shape, while the membrane of lowest elastic stiffness demonstrates unstable interactions between its inflated shape and the resulting unsteady wake. These unstable effects are shown to be significantly magnified by the flexible nature of the membrane compared with a rigid surface of the same average shape. Copyright © 2007 John Wiley & Sons, Ltd.

Received 11 May 2007; Revised 10 October 2007; Accepted 14 October 2007

KEY WORDS: fluid–structure interaction; elastic membrane structure; Navier–Stokes equations; moving mesh finite volume method

1. INTRODUCTION

Coupled membrane–fluid systems are found in many fields of scientific design and research such as heart valves [1], blood cells [2], parachutes [3], airbags [4], sails [5], membrane airfoils for micro-air vehicles [6] and lightweight fabric building structures [7].

*Correspondence to: Deborah M. Greaves, Department of Architecture & Civil Engineering, University of Bath, Bath BA2 7AY, U.K.
†E-mail: absdmg@bath.ac.uk, d.m.greaves@bath.ac.uk

The investigation of this highly coupled fluid–structure system presents a significant challenge to both experimental and numerical fluid dynamicists. One significant characteristic of the system is the flexibility of the membrane, which causes it to undergo large displacements and deformations under the applied fluid load. Since the membrane represents an internal (most often impermeable) boundary to the flow, as its shape changes, the flow around the membrane changes, thus altering the forces on the membrane in a continuous feedback loop. Separation from the curved membrane surface may occur which also changes the forces on the structure. These effects may eventually combine to cause the membrane and flow regime to come into equilibrium in a steady stable state, or alternatively non-steady behaviour could result, which may be composed of many superimposed structural modes interacting with a highly unsteady wake.

Coupled membrane–fluid dynamics is difficult to investigate experimentally. Significant challenges include the application of structure boundary conditions, for example, a fixed leading edge, without disturbing flow in the vicinity, and instrumentation of the model without interfering with the flexibility of the surface. In a numerical investigation, in addition to the realistic reproduction of the behaviour of each system (fluid and structure) the accurate modelling of the interactions at the interface between the two media is of the utmost importance to ensure global energy conservation of the coupled system. The fluid numerical model must be suitable for simulations with complex-shaped moving boundaries, thus employing in general either a body-fitted moving grid [8], or a stationary Eulerian approach such as the immersed boundary method [9]. Algebraic mesh moving methods relate the motion of the internal mesh nodes to the motion of the boundary nodes via an algebraic expression, for example, using a *master/slave* strategy [10]. Alternatively, the mesh may be considered to be a structure in its own right, and a solution to the equations of elasticity sought, as in the pseudo-solid approach [11], or a discrete spring analogy may be used [12, 13]. Suitable distribution of computational nodes is required to capture the relevant detail of the flow, and if a body-fitted grid is used a grid moving technique that maintains grid quality over time is required. The structure material model must be suitable for large strains and may be required to incorporate non-linear material characteristics, for example, in the case of a woven sail fabric.

Considering the coupled system, if non-matching grids are used an interpolation at the interface must be carefully designed to transfer information between the two sets of data—fluid to structure and structure to fluid. Time dependency of the system presents a further challenge since the method must accurately render the unsteady coupled interactions. The popular approach of a quasi-unsteady analysis [14, 15], in which sail inertia is neglected and a static equilibrium shape found within each timestep is unlikely to be suitable since the fluid 'sees' the structure as a rigid stationary body in its current configuration. In the present case, however, due to the relatively low mass of the membrane, not only its position but also its velocity (rate of change of position) is significant, neither of which are known *a priori*, but instead must be found as part of the solution.

Many researchers have taken advantage of the reduced computational complexity offered by potential flow-based methods, such as the vortex lattice method, to tackle the modelling of membrane–fluid systems. In these cases the effects of viscosity are neglected [15, 16], which restricts the model to cases where boundary layer effects such as separation are unlikely to be significant. Alternatively, additional assumptions or empirical information are used to provide a 'viscous correction', for example, to model a leading edge separation bubble [17], or trailing edge separation [18]. Most often this requires additional assumptions to be made about the flow, for example, that the boundary layer remains attached downstream of the leading edge separation bubble or that the oncoming flow is tangential to the leading edge of the membrane (ideal incidence).

DOI: 10.1002/fld

For small angles of attack and membranes of small camber (due to small excess length ratio) viscous effects play a less significant role since large regions of separated flow do not occur. In these cases reasonable agreement between potential flow-based models and experimental data has been found [19]. However, outside of these tolerances the results rapidly deviate from the potential flow-based predictions. Significant discrepancies in force coefficients even for membranes of small camber only a few degrees from zero angle of attack have been found [19]. As highlighted by Newman [20], these discrepancies are widely accepted to be due to viscous effects.

While the presence of viscosity will induce shear stresses on the surface of the membrane thus altering its tension, the more significant boundary layer effect is the change in surface pressure distribution. The second effect is more significant because the pressure distribution, or more specifically the net pressure difference between the membrane's upper and lower surface, has more influence over the membrane shape.

2. NUMERICAL MODEL

In these two-dimensional analyses an unstructured triangular grid [21] is used to enable the complex-shaped domain to be meshed in a relatively straightforward manner, with no special mesh treatment required at the boundary. All computational volumes have the same topology, which simplifies the data structure and computer code. An unstructured approach also allows mesh nodes to be concentrated in regions of interest easily and efficiently, such as in the boundary layer near the membrane. A collocated finite volume method is used to discretize the fluid equations of motion. The structure is discretized as a set of one-dimensional straight links in a Lagrangian approach. The motion of the fluid–structure boundary causes motion of all mesh nodes so that the mesh adapts and remains fitted to the boundary. This approach ensures that the topology of the mesh remains constant throughout the simulation, and so neighbour finding routines, which are computationally expensive on unstructured meshes, are only carried out once at the beginning of the simulation. Furthermore, re-meshing of the domain is avoided, which is also computationally expensive and can introduce errors during the interpolation of the flow field from one mesh to the next.

2.1. Discretization of the fluid equations of motion

The differential equations of motion describing the unsteady flow of an incompressible Newtonian fluid are

$$\rho\frac{\partial \mathbf{U}}{\partial t}+\rho\nabla\cdot(\mathbf{U}\mathbf{U})=\mu\nabla^2\mathbf{U}-\nabla p \tag{1}$$

and

$$\nabla\cdot\mathbf{U}=0 \tag{2}$$

in which ρ is the density and μ is the dynamic viscosity of the fluid, $\mathbf{U}$ is the vector of fluid velocity, p is the pressure and t is the time. If the point of interest, P, at which the equations of

DOI: 10.1002/fld

motion are evaluated, is moving with an arbitrary velocity **W**, then the momentum equation (1) contains an extra term:

$$\rho\frac{\delta \mathbf{U}}{\delta t}+\rho\nabla\cdot(\mathbf{U}\mathbf{U})-\rho\mathbf{W}\cdot(\nabla\mathbf{U})=\mu\nabla^2\mathbf{U}-\nabla p \tag{3}$$

The continuity equation (2) remains unchanged. The temporal derivative in Equation (1) is the rate of change seen by a 'stationary' observer. The temporal derivative in Equation (3) is the rate of change as seen by an observer moving with the velocity vector field **W**. The two derivatives are related according to

$$\frac{\delta(\mathbf{U})}{\delta t}=\frac{\partial(\mathbf{U})}{\partial t}+\mathbf{W}\cdot(\mathbf{U}) \tag{4}$$

which has been used in the derivation of Equation (3).

Following the finite volume approach, the momentum equations (3) are integrated over a moving triangular control volume shown in Figure 1. The unknown variables of pressure and two components of velocity are stored at its moving centroid and are considered to represent the average over the control volume, thus Equation (3) gives

$$\rho\frac{\mathrm{d}}{\mathrm{d}t}\left(\int_V \mathbf{U}\,\mathrm{d}V\right)+\rho\int_V \nabla\cdot((\mathbf{U}-\mathbf{W})\mathbf{U})\,\mathrm{d}V=\mu\int_V \nabla^2\mathbf{U}\,\mathrm{d}V-\int_V \nabla p\,\mathrm{d}V \tag{5}$$

in which the time-dependent term integral

$$\rho\int_V \frac{\delta \mathbf{U}}{\delta t}\,\mathrm{d}V=\rho\frac{\mathrm{d}}{\mathrm{d}t}\left(\int_V \mathbf{U}\,\mathrm{d}V\right)-\rho\int_V \mathbf{U}\frac{\delta(\mathrm{d}V)}{\delta t} \tag{6}$$

the vector identity

$$\mathbf{W}\cdot(\nabla\mathbf{U})=\nabla\cdot(\mathbf{W}\mathbf{U})-(\nabla\cdot\mathbf{W})\mathbf{U} \tag{7}$$

and the definition of volumetric strain

$$\frac{\delta(\mathrm{d}V)}{\delta t}=(\nabla\cdot\mathbf{W})\,\mathrm{d}V \tag{8}$$

have all been used for simplification. After further simplification using the divergence theorem, Equation (5) becomes

$$\rho\frac{\mathrm{d}}{\mathrm{d}t}\left(\int_V \mathbf{U}\,\mathrm{d}V\right)+\rho\int_S \mathrm{d}\mathbf{S}\cdot((\mathbf{U}-\mathbf{W})\mathbf{U})=\mu\int_S \mathrm{d}\mathbf{S}\cdot(\nabla\mathbf{U})-\int_S p\,\mathrm{d}\mathbf{S} \tag{9}$$

the x-component of which can be expressed as

$$\rho\frac{\mathrm{d}}{\mathrm{d}t}\left(\int_V U^x\,\mathrm{d}V\right)+\rho\int_S((\mathbf{U}-\mathbf{W})U^x)\,\mathrm{d}\mathbf{S}=\mu\int_S(\nabla U^x)\,\mathrm{d}\mathbf{S}-\int_S p\mathbf{i}\,\mathrm{d}\mathbf{S} \tag{10}$$

in which U^x is the component of velocity in the x-direction.

The *time-dependent term* is discretized using a first-order backward Euler stencil:

$$\rho\frac{\mathrm{d}}{\mathrm{d}t}\left(\int_V U^x\,\mathrm{d}V\right)\cong\rho\left(\frac{V^{t+1}U^{x^{t+1}}-V^tU^{x^t}}{\Delta t}\right)_P \tag{11}$$

DOI: 10.1002/fld

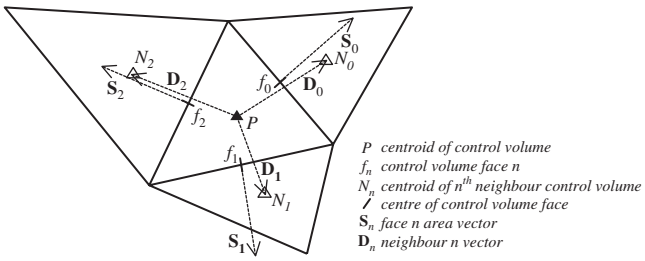

Figure 1. Triangular fluid control volume with neighbour volumes and associated geometry.

The *convection term* is simplified using the midpoint rule to convert the surface integral to a discrete sum over the volume faces, and then linearized by treating the mass flux through the face explicitly, giving the convective flux through one face as

$$\rho A_f U_f^x((\mathbf{U}_f - \mathbf{W}_f)\cdot\mathbf{n}_f) = m_f U_f^x \tag{12}$$

in which the explicit flux m_f is calculated using the Rhie–Chow interpolation [22] as described shortly.

The *diffusion term* is simplified using the midpoint rule to convert the surface integral to a discrete sum over the volume faces, and then the correction of Muzaferija [23] is applied to take into account the non-orthogonality of the grid, giving the diffusive flux through one face as

$$\mu A_f((\nabla U^x)_f\cdot\mathbf{n}_f) = \mu A_f\left[\left(\frac{U_N^x - U_P^x}{|\mathbf{D}_f|}\right)(\mathbf{d}_f\cdot\mathbf{n}_f) + ((\overline{\nabla U^x})_f - ((\overline{\nabla U^x})_f\cdot\mathbf{d}_f)\mathbf{d}_f)\cdot\mathbf{n}_f\right] \tag{13}$$

where the overbar terms are linearly interpolated from the computational nodes either side of the face, the control volume centre node gradient terms are calculated using the divergence theorem:

$$(\nabla U^x)_P = \frac{1}{V_P}\sum_f \overline{U_f^x}\mathbf{S}_f \tag{14}$$

and $\mathbf{d}$ is the unit vector between P and its neighbour N across side f

$$\mathbf{d}_f = \frac{\mathbf{D}_f}{|\mathbf{D}_f|} \tag{15}$$

in which $\mathbf{D}_f$ is as defined in Figure 1. The second term in the square brackets in Equation (13) is treated explicitly.

The *pressure gradient term* is simplified using the midpoint rule, the contribution of one face to the resulting discrete sum is

$$p_f(\mathbf{i}\cdot\mathbf{S}_f) = p_f A_f n_f^x \tag{16}$$

To complete the discretization, the power law scheme is used to interpolate the unknown face velocity in Equation (12) according to the local Peclet number of the control volume face, which is defined as

$$Pe_f = \frac{m_f|\mathbf{D}_{PN}|}{\mu A_f(\mathbf{d}_f\cdot\mathbf{n}_f)} \tag{17}$$

DOI: 10.1002/fld

The x-direction component of the discretized momentum equations is now given by

$$a_P U_P^x = \sum_f a_N U_N^x + b_P \tag{18}$$

in which

$$a_N = \frac{\mu A_f}{|\mathbf{D}_{PN}|}(\mathbf{d}_f \cdot \mathbf{n}_f) g(|Pe_f|) + \max(0, -m_f) \tag{18a}$$

$$a_P = \frac{\rho V_P}{\Delta t} + \sum_f (a_N + m_f) \tag{18b}$$

$$b_P = \frac{\rho V_P U_P^{x^t}}{\Delta t} + \mu \sum_f A_f D_{\text{cross}}^x - \sum_f p_f A_f n_f^x \tag{18c}$$

where

$$g(|Pe_f|) = \max(0, (1 - 0.1|Pe_f|)^5) \tag{19}$$

in which $|Pe_f|$ is the magnitude of the face Peclet number defined in Equation (17), and

$$(D_{\text{cross}}^x)_f = ((\overline{\nabla U^x})_f \cdot \mathbf{n}_f) - ((\overline{\nabla U^x})_f \cdot \mathbf{d}_f)(\mathbf{n}_f \cdot \mathbf{d}_f) \tag{20}$$

is the explicit cross-diffusion correction from Equation (13).

The explicit mass flux term in Equation (12) is calculated using the Rhie–Chow method [22] which interpolates the pressure and velocity terms independently

$$m_f = \rho A_f ((\overline{\mathbf{U}}_f - \mathbf{W}_f) \cdot \mathbf{n}_f) + \rho A_f \overline{\left[\frac{V_P}{a_P}\right]}_f ((\overline{[(\nabla p)_P]}_f - (\nabla p)_f) \cdot \mathbf{n}_f) \tag{21}$$

in which a_P is as defined in Equation (18a), the overbar again represents linear interpolation, and the centre node gradient terms are calculated according to Equation (14). The direct face pressure gradient is evaluated as

$$(\nabla p)_f = \left(\frac{p_N - p_p}{|\mathbf{D}_{PN}|}\right) \mathbf{d}_{PN} \tag{22}$$

It is clear that Equation (8) represents a differential form of the integral geometric conservation law [24], and its satisfaction has been implied in the simplifications applied to the integration of Equation (3). Furthermore, the convective fluxes are evaluated at the midpoint between t and $t+1$ which is consistent with the first-order backward time differencing and midpoint rule approximations used here [25].

The SIMPLE algorithm of Patankar and Spalding [26] is used to introduce a pressure correction equation using the equation of conservation of mass (continuity equation) equation (2). The velocities found from solution of the momentum equations (18) will in general, during the solution procedure, not satisfy continuity of mass since the divergence-free condition is not implied in the momentum equations and the pressure field used in their calculation is treated explicitly. If the

DOI: 10.1002/fld

velocities and pressures are considered to be made up of an initial guess and a correction, the discretized continuity equation (2) becomes

$$a_{Pp'} p'_P = \sum_N a_{Np'} p'_N + b_{Pp'} \tag{23}$$

where p' is the pressure correction required, and the following coefficients apply:

$$a_{Np'} = A_f \overline{\left[\frac{V_P}{a_P}\right]}_f \left(\frac{\mathbf{d}_{PN} \cdot \mathbf{n}_f}{|\mathbf{D}_{NP}|}\right) \tag{23a}$$

$$a_{Pp'} = \sum_N a_{Np'} \tag{23b}$$

$$b_{Pp'} = -\sum_f A_f (\overline{\mathbf{U}^*_f} \cdot \mathbf{n}_f) \tag{23c}$$

Considering the definition of face mass fluxes, the pressure correction source term equation (23c) can be considered as

$$b_{Pp'} = -\frac{1}{\rho} \sum_f \overline{m^*_f} \tag{24}$$

Since the mass fluxes in Equation (24) are evaluated using interpolated velocities, the Rhie–Chow correction described previously is also used here.

Once Equation (23) has been solved for the pressure corrections, the velocity corrections are calculated by

$$u'_P = -\frac{V_P}{a_P} ((\nabla p')_P \cdot \mathbf{i}) \tag{25}$$

wherein the method equivalent to Equation (14) is used for the evaluation of pressure correction gradients. The velocities and pressure are then corrected according to

$$\mathbf{U}_P = \mathbf{U}^*_P + \mathbf{U}'_P \tag{26a}$$

and

$$p_P = p^*_P + p'_P \tag{26b}$$

where the star indicates a 'guessed' variable, in this case the velocity found after solution of the momentum equations and the pressure used for that solution.

An iterative approach to the solution of the momentum equations (18) is adopted. To aid stability, the velocities are over-relaxed:

$$u^{t+1}_P = (1 - \alpha_{\text{vel}}) u^t_P + \alpha_{\text{vel}} \left[\frac{\sum_N a_N u_N + b_P}{a_P}\right] \tag{27}$$

where α_{vel} is the velocity over-relaxation factor, chosen between 0 and 1, which effectively finds the new velocity as a blend of the velocity at the previous timestep and the velocity calculated by Equation (18). The same factor is used for both x- and y-momentum calculations. The velocity

DOI: 10.1002/fld

relaxation is duly taken into account in the calculation of the explicit Rhie–Chow mass fluxes as described previously where Equation (21) becomes

$$m_f = \rho A_f (\mathbf{U}_f \cdot \mathbf{n}_f) = \rho A_f (\overline{\mathbf{U}}_f \cdot \mathbf{n}_f) + \rho A_f \alpha_{\text{vel}} \overline{\left[\frac{V_p}{a_P}\right]}_f [(\overline{((\nabla p)_P)}_f - (\nabla p)_f) \cdot \mathbf{n}_f] \tag{28}$$

and in the calculation of the velocity corrections where Equation (25) becomes

$$u'_P = -\alpha_{\text{vel}} \frac{V_P}{a_p} \left(\frac{\partial p'}{\partial x}\right)_P \tag{29}$$

The correction to the pressure is under-relaxed to compensate for the simplifying assumptions made in the formulation of the pressure correction equation. Equation (26b) becomes

$$p_P = p^*_P + \alpha_p p'_P \tag{30}$$

where α_p is the pressure under-relaxation factor that damps the rate of change of the pressure field.

Conditions on velocities and pressure at the boundaries of the domain are imposed through the use of 'mirror nodes'; a fictitious node outside the domain boundary, one for each boundary fluid control volume. The value of the variable at the mirror node is set so that interpolations to the face of the volume on the boundary produce the required condition. The boundary node is located such that the vector *PN* on that side passes through the centre of the boundary face in order to maximize the accuracy of the midpoint rule approximations. The non-orthogonalities are taken into account in the same manner as for internal volume faces.

2.2. *Discretization of the structure equations of motion*

The structure is discretized as a set of straight links with zero thickness, which is a sub-set of the fluid mesh edges. A Lagrangian approach is taken in which the structure mass is lumped at the link nodes and a spring and dashpot system connects the nodes together in a chain along the length of the membrane. Considering the equilibrium of a structure node shown in Figure 2:

$$M_P \left(\frac{\dot{\mathbf{X}}^{t+1}_P - \dot{\mathbf{X}}^t_P}{\Delta t}\right) = \mathbf{R}_P \tag{31}$$

in which M_P is the mass, $\mathbf{X}_P$ the coordinates and $\mathbf{R}_P$ the out of balance force associated with structure node P. The resultant force $\mathbf{R}$ is made up of internal structure forces and external applied fluid forces. Internal structure forces are those due to the elastic deformation of the structure and those due to internal damping of its motion.

The *internal elastic forces* are evaluated by considering the deformations of the structure from its original (unstressed state) to determine the tension in each structure segment. To aid stability, a new elasticity model is introduced which uses a blend of local and global elastic effects at each structure node:

$$\begin{aligned} T^{\text{e}} &= T^{\text{e}}_{\text{local}} + T^{\text{e}}_{\text{global}} \\ &= EA \left[\theta \frac{L_{PN} - L^0_{PN}}{L^0_{PN}} + (1-\theta)\frac{L - L^0}{L^0}\right] \end{aligned} \tag{32}$$

DOI: 10.1002/fld

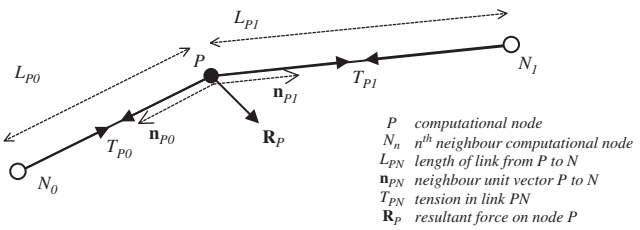

Figure 2. Structure computational node and associated geometry.

in which EA is the product of the material elastic modulus and the cross-sectional area of the discrete link connecting P to neighbour node N, and L_{PN} and L^0_{PN} are the current and unstressed length of that link. L and L^0 are the current and unstressed length of the membrane as a whole, and θ is a blending factor equal to $1/n$ where n is the discretization of the membrane.

The *internal damping force* is evaluated by considering the relative velocity between the two ends of the structure segment at P and N. The damping contribution to structure segment tension is

$$T^{\mathrm{d}} = C(\dot{\mathbf{X}}_N - \dot{\mathbf{X}}_P) \cdot \mathbf{n}_{PN} \tag{33}$$

in which C is a damping coefficient and $\mathbf{n}_{PN}$ is the unit vector between P and N (see Figure 2).

The *external applied forces* are those due to the actions of the fluid on the membrane and are made up of a pressure component and a viscous component. To be conservative in this interface interaction, the force applied to a given structure segment must be equal and opposite to that felt by the adjacent fluid control volume due to the presence of the structure. This is achieved by recording the force applied to this control volume face during the solution of the momentum equations (18) in both x- and y-directions. Equal and opposite forces are thus taken to act on the structure segment coincident with this control volume face, and these force components are then interpolated to the structure nodes at either end of the segment.

Once the resultant force on a given structure node has been evaluated (both internal and external effects), Equation (31) is solved to find the new nodal velocity, and the coordinates of the node are updated according to

$$x_P^{t+1} = x_P^t + \Delta t \dot{x}_P^{t+1} \tag{34a}$$

and

$$y_P^{t+1} = y_P^t + \Delta t \dot{y}_P^{t+1} \tag{34b}$$

in which $[x, y]$ and $[\dot{x}, \dot{y}]$ are, respectively, the coordinates and velocities of structure node P in the component form.

2.3. Mesh motion control

As the structure position is updated each timestep, so the fluid mesh nodes must also be updated to maintain a body-fitted mesh of sufficient quality. A pseudo-structural approach is used here to control mesh motion in which the membrane structure displacements drive a system of equations describing the equilibrium of each mesh node. The change in position of the mesh nodes is

DOI: 10.1002/fld

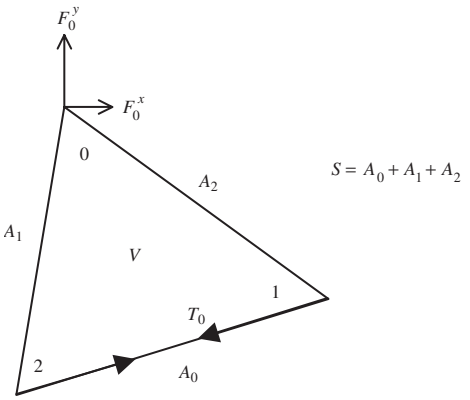

Figure 3. Mesh triangle geometry relating to mesh moving algorithm.

calculated in a similar manner to the motion of the structure nodes considering the links of the mesh to be structural elements. The resultant force at each mesh node $\mathbf{R}_P$ contains terms relating only to the deformation of the mesh. The material model used to derive these internal mesh forces from the mesh deformations is fictitious, and can be manipulated to control the performance of the mesh as desired. In this work the mesh forces have an edge tension component and a shape component as follows.

The *edge tension* component is found by considering each link of the mesh to be a linear elastic spring having a constant tension coefficient (C_T), which relates the tension in the link to its length. Considering node 0 in Figure 3

$$T_0 = C_\mathrm{T} A_0 \tag{35}$$

The overall effect of a constant tension coefficient (corresponding to a zero slack length) is to cause the mesh node to move towards the geometric centre of all the nodes to which it is connected by a mesh link.

The *shape force* is evaluated triangle by triangle, and its components applied to each apex node in turn. In the component form, for the mesh triangle shown in Figure 3, the shape forces at node 0 are

$$F_0^x = C_\mathrm{S}\left[\frac{2}{S}\left(\frac{x_1 - x_0}{A_2} + \frac{x_2 - x_0}{A_1}\right) - \frac{y_2 - y_1}{2V}\right] \tag{36a}$$

and

$$F_0^y = C_\mathrm{S}\left[\frac{2}{S}\left(\frac{y_1 - y_0}{A_2} + \frac{y_2 - y_0}{A_1}\right) - \frac{x_2 - x_1}{2V}\right] \tag{36b}$$

in which x_0, y_0, etc. are the coordinates of the triangle nodes, V is the triangle volume, A_0, etc. are the triangle face areas and S is the triangle perimeter. C_S is a constant shape coefficient. The first term in square brackets in Equations (36a) and (36b) has the effect of moving the nodes towards minimizing the difference in length between the three sides of the triangle. The second term represents the resultant at the node of an internal pressure in the triangle which is inversely proportional to its volume, thus when the effects of all triangles meeting at node 0 are taken into

DOI: 10.1002/fld

account, the resultant effect is to move node 0 in such a way as to reduce differences in volumes between these triangles. This second term provides the mesh with a compressive resistance. Use of the edge tension coefficient controls mesh motion and the shape coefficient ensures that no zero area triangles occur in the mesh.

Once the tensions in all the mesh links meeting at mesh node P and the shape forces due to all the mesh triangles meeting at mesh node P are known, the resultant force at P can be evaluated and the change in mesh nodal positions are given by

$$\delta x_P^{t+1} = \alpha_m \frac{R_P^x}{K_P} + \beta_m \delta x_P^t \tag{37a}$$

and

$$\delta y_P^{t+1} = \alpha_m \frac{R_P^y}{K_P} + \beta_m \delta y_P^t \tag{37b}$$

in which α_m and β_m are mesh iteration relaxation factors. The nodal stiffness K_P also consists of an edge component and a shape component given, referring again to node 0 in Figure 3, by

$$K_0 = C_T + \frac{10C_S}{4}\left[\frac{2}{S^2 A_1 A_2}(2A_1^2 + 2A_2^2 + A_0(A_1 + A_2 - A_0)) + \frac{2A_0^2}{4V^2}\right] \tag{38}$$

The positions of mesh nodes not coincident with any domain boundary (including the membrane structure) are then updated accordingly. The mesh motion equations are solved iteratively until a predefined level of static equilibrium (judged according to the kinetic energy of the mesh) is reached. Thus, the mesh 'material' parameters C_T and C_S determine the response of the mesh elements to deformation, and the mesh iteration parameters α_m and β_m control the convergence of the mesh into its equilibrium position.

Overall, an iterative approach is taken to the solution of each equation set. The structure, mesh and then fluid equations of motion are solved in a sequentially staggered manner, projecting each system in turn forward in time. An unsteady approach is used, which tracks the interactions of the fluid and the structure over time; complex unsteady motions will be observed and a stable static shape may or may not be found in each case.

3. RESULTS

3.1. Validation tests

The test case of flow past a normal flat plate is used to test the ability of the approach to model a zero thickness internal boundary (including a significant pressure difference across the boundary), separation of the flow with regions of strong recirculation, evaluation of forces on an internal structure in the flow and to evaluate the accuracy of the algorithm on stationary and moving meshes in both steady and unsteady formulations.

A flat rigid plate of zero thickness is held normal to a uniform flow as shown in Figure 4. The Reynolds number is defined with respect to the plate height, and a selection of cases in the range $Re = 1.2$–18 are studied. The length of the recirculating vortices, as shown in Figure 4,

DOI: 10.1002/fld

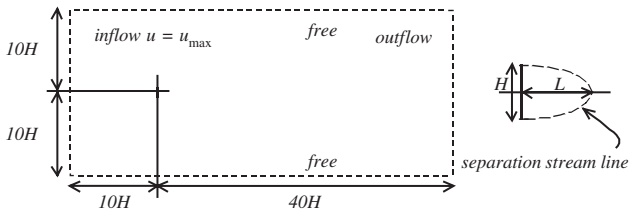

Figure 4. Domain geometry, boundary conditions and wake parameters for flow past a normal flat plate test cases.

non-dimensionalized with respect to the plate height, and the drag forces felt by the plate are compared with the available data. The drag coefficient is defined as

$$C_{\mathrm{D}} = \frac{2F^x}{\rho u_{\max}^2} \tag{39}$$

where F^x is the net force on the plate in the x-direction.

Owing to its zero thickness, the flat plate experiences only pressure drag (or form drag) induced by the pressure difference between its two sides. The mesh has 28 elements on each face of the plate, which gives 19 872 elements in total. The meshes are refined in the area around the tips of the plate and in the wake by placing extra mesh edges there in the mesh generating process. The velocity over-relaxation factor is 0.8 (Equation (27)), the under-relaxation factor on pressure update is 0.02 (Equation (30)) and the non-dimensional timestep is 0.25. The initial conditions are zero pressure and maximum oncoming velocity at all internal nodes. The no-slip condition is imposed on the mesh edges coincident with the plate.

Figure 5 shows the variation of non-dimensionalized eddy length with Reynolds number, in comparison with published data; the results demonstrate a clear agreement, particularly with the work of Hudson and Dennis [27] and Dennis *et al*. [28], who use a finite difference approach on a polar grid, in a primitive variable and stream function–vorticity formulation, respectively. The variation of drag coefficient with Reynolds number is shown in Figure 6, also demonstrating good agreement with published data.

Next an arbitrary mesh motion is imposed during the solution in order to test the effect of errors in geometric conservation. In a case such as this with distinct separation and recirculation, such errors could have a significant impact on the flow structure and therefore also on the forces felt by the plate.

The arbitrary mesh motion is generated by superimposing a random time-varying perturbation on all internal mesh nodes, the maximum perturbation being 30% of the smallest mesh edge length to avoid mesh tangling. Over time, no net translation of the control volumes occurs, and the movement can be thought of as a vibration of the mesh edges causing distortion of the control volumes. This is a harsh mesh motion test, since the motion of any one mesh edge is completely independent of the motion of the edges around it, and is independent from one iteration or timestep to the next.

The Reynolds number 18 flow is modelled with the same initial and boundary conditions, relaxation parameters and timestep as the stationary mesh case described previously. Both steady

DOI: 10.1002/fld

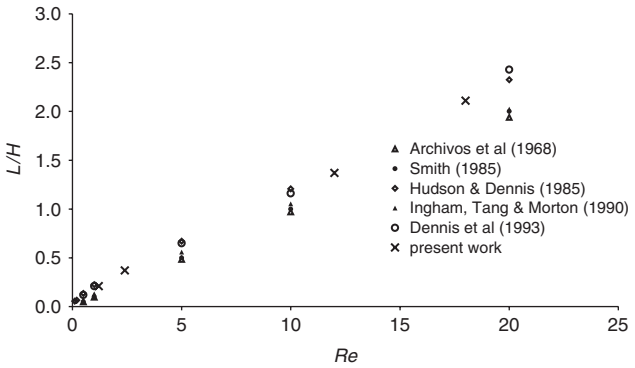

Figure 5. Variation of non-dimensionalized eddy length with *Re*, flow past a normal flat plate. Comparison with data from Archivos *et al*. [29], Smith [30], Hudson and Dennis [27], Ingham *et al*. [31] and Dennis *et al*. [28].

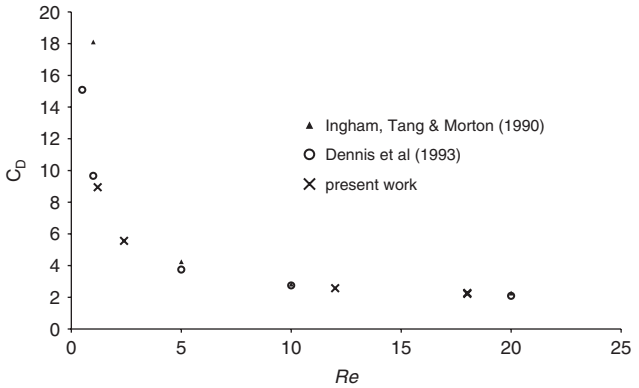

Figure 6. Variation of drag coefficient with *Re*, flow past a normal flat plate. Comparison with data from Ingham *et al*. [31] and Dennis *et al*. [28].

and unsteady formulations are used; in the steady formulation, the mesh motion is imposed on each iteration, in the unsteady formulation, the nodes are moved at the beginning of each timestep.

The drag coefficient, as defined by Equation (39) is monitored, for both the steady and unsteady formulations on both the stationary and arbitrarily moving meshes. Excellent agreement is demonstrated between the steady and unsteady formulations, and between the stationary and moving mesh cases with all four cases giving a value $C_D = 2.29$–2.30.

3.2. Elastic membrane cases

The model described in Section 2 and validated in Section 3.1 is applied to the two-dimensional test case of modelling the unsteady motions of an elastic membrane moving from an initial flat and unstressed state to a curved profile as a result of the aerodynamic forces on the membrane.

DOI: 10.1002/fld

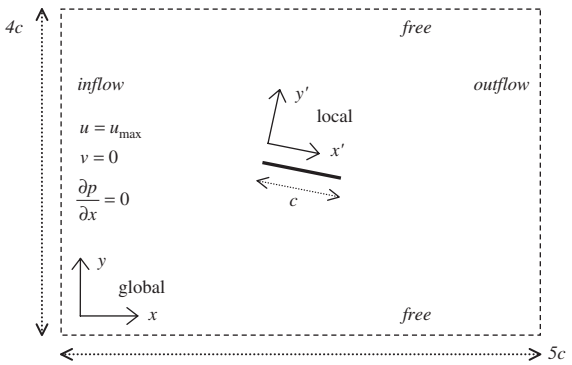

Figure 7. Domain geometry, boundary conditions and membrane parameters for flow around an elastic membrane test cases, including global and local coordinate system definitions.

An angle of attack of 4° is used and the Reynolds number is based on the chord length, c, of the membrane (the distance between its two fixed ends):

$$Re = \frac{\rho U c}{\mu} \tag{40}$$

in which ρ is the fluid density, U is the oncoming flow velocity and μ the fluid viscosity. The Reynolds number of the problem here is set to 4000 and the computational domain and boundary conditions are shown in Figure 7.

Following Shyy and Smith [8], an additional non-dimensional parameter is introduced describing the relative stiffness of the membrane:

$$\Pi = \sqrt[3]{\frac{EA}{q_\infty c}} \tag{41}$$

in which q_∞ is the stagnation pressure of the flow defined as

$$q_\infty = \tfrac{1}{2}\rho U^2 \tag{42}$$

Internal damping of 1% of critical is applied (Equation (33)), and the damping factor C is calculated according to

$$C = 0.02\sqrt{s_{PN} M_P} \tag{43}$$

where s_{PN} is the axial stiffness of the membrane segment:

$$s_{PN} = \frac{EAn}{L^0} \tag{44}$$

in which the membrane has original (unstressed) length L^0 and is discretized into n segments, and M_P is the structure nodal mass:

$$M_P = \rho_s^0 \frac{L^0}{n} \tag{45}$$

in which ρ_s^0 is the original linear density of the structure.

DOI: 10.1002/fld

Furthermore, considering the relative densities of the fluid and the structure, the ratio

$$M = \frac{\rho_s^0 c}{\rho c^2} \tag{46}$$

in this work is set to 2.0. Since gravitational effects are neglected, the linear density of the structure will not affect the final equilibrium shape of the membrane, but it will govern its motion over time towards this shape.

For the fluid solver, a non-dimensional timestep of 0.001 is combined with a pressure relaxation factor of 0.8 (Equation (30)) and a velocity relaxation factor of 0.8 (Equation (27)). In the mesh moving model, a combination of $C_T = 0.1$ (Equation (35)) and $C_S = 0.001$ (Equations (36a) and (36b)) is used, along with $\alpha_m = 0.25$ and $\beta_m = 0.9$ (Equation (37)). These values are arrived at by trial and error to achieve a stable computation.

The simulations are run until changes in the lift and drag forces on the membrane have reached steady values, which in general occurs after 35 non-dimensional seconds, although each case is judged individually.

3.2.1. Mesh dependency test. To test the dependency of the results on the fineness of the mesh, simulations are carried out having 100, 200 and 400 structural segments on the membrane. Since the fluid mesh is body fitted to the structure, this also governs the fineness of the fluid mesh in the vicinity of the structure. Figure 8 shows the fluid mesh for the case of 100 segments on the membrane. A zone of mesh refinement is generated by seeding mesh nodes along a line projected upstream of the leading edge for a distance of 10% of the chord length c, and downstream for a distance of 50% of c.

The distribution of elasticity in the structure between local and global effects is adjusted to take into account the reduction in local segment length according to Equation (32) since θ is dependent on the structure discretization n as previously described. The membrane has an EA of 2.7e8 resulting in $\Pi = 15$ (Equation (41)). The evolution over time of the drag and lift forces

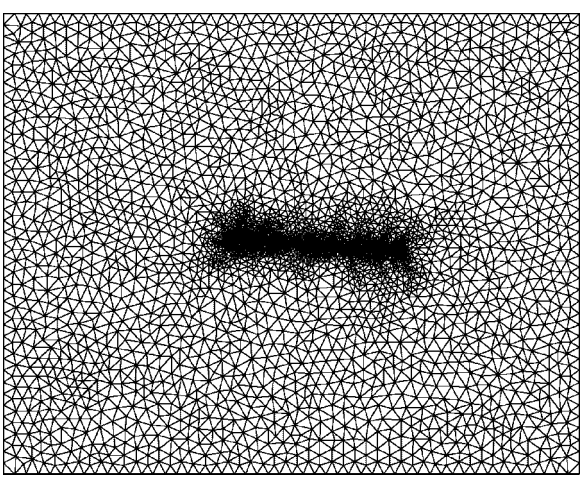

Figure 8. Computational mesh with 100 segments on the membrane surface.

DOI: 10.1002/fld

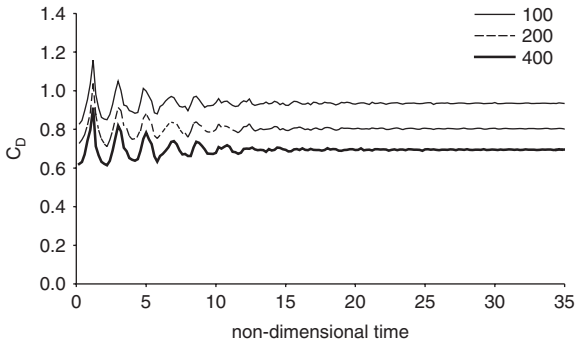

Figure 9. Time history of drag coefficient for $\Pi = 15$ membranes, 100, 200 and 400 segments on the membrane surface.

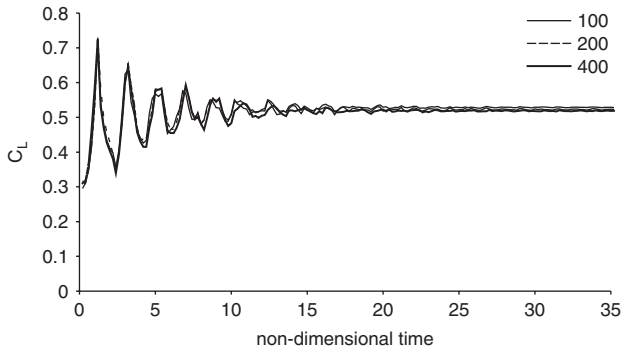

Figure 10. Time history of lift coefficient for $\Pi = 15$ membranes, 100, 200 and 400 segments on the membrane surface.

felt by the membrane are shown in Figures 9 and 10, respectively. Drag is the force felt by the membrane in the global x-direction and lift acts in the global y-direction (see Figure 7).

It can be seen from Figure 9 that the total drag is not mesh independent at this stage, although mesh convergence is demonstrated in that the change in drag coefficient reduces as the mesh becomes finer. If we consider the forces that make up this drag force, we can identify the part of the model most affected by the mesh refinement, as demonstrated in Figure 11. It can be seen that the pressure drag is almost identical in each of the three cases and that the difference in drag coefficient demonstrated in Figure 9 is almost entirely due to the difference in viscous drag between the three cases. It is to be expected that the viscous drag dominates the pressure component since the structure surface area is predominantly aligned with the flow direction. Since calculation of viscous stresses relies on the evaluation of velocity gradients, it is clear here that differences in drag between the cases are due to increasing accuracy of velocity gradient modelling near the fluid–structure interface. This is to be expected considering that the more fine the mesh, the more computational points are clustered in the boundary layer region in the direction normal to the membrane surface, and thus the more accurate the reconstruction of the velocity profile (and hence the velocity gradient and rate of change of gradient) in this direction. The same effect is

DOI: 10.1002/fld

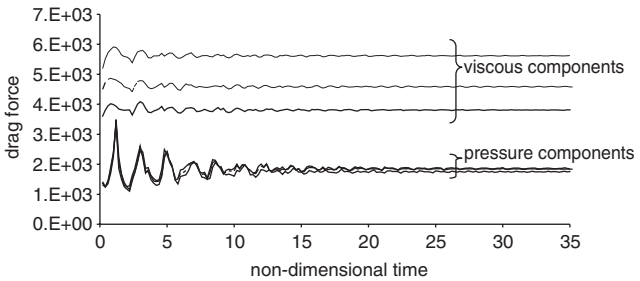

Figure 11. Time history of drag force viscous and pressure components for $\Pi = 15$ membranes, 100, 200 and 400 segments on the membrane surface (legend as Figure 10).

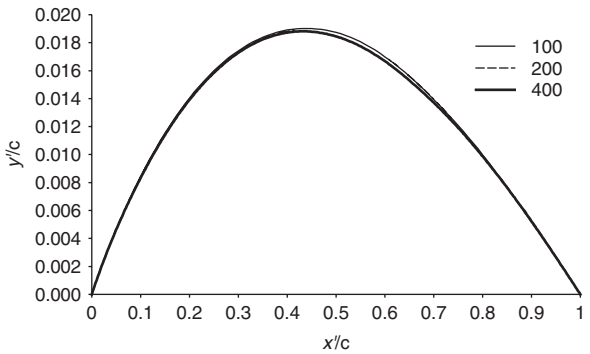

Figure 12. Membrane profile at non-dimensional $t = 35$, for $\Pi = 15$ membranes, 100, 200 and 400 segments on the membrane surface.

demonstrated in the results for lift coefficient when the viscous component is inspected; however, since the lift force is dominated by the pressure contribution, the total lift coefficient remains largely unchanged as shown in Figure 10.

Considering the steady shape that the membrane adopts, Figure 12 plots the membrane profile in each case at non-dimensional $t = 35$, in which the coordinates of the nodes of the membrane have been transformed into local coordinates with local x aligned with the chord of the membrane and local y perpendicular to it (see Figure 7). The figure shows that only very slight differences are found between different cases, and therefore the differences in overall drag felt by the membrane are due to differences in the forces at the fluid–structure interface, rather than differences in geometry of the surface. Pressure difference between the top and bottom surface is the primary driver of shape changes in the membrane, and therefore, since pressure components of the aerodynamic forces are very similar across the three cases, it is to be expected that the shapes adopted by the membranes will be very similar also, as is the case. This supports the argument that differences in the overall drag on the membrane is due to the accuracy of velocity gradient reconstruction in the boundary layer.

For computational efficiency, the 100-segment model is taken forward to investigate other membranes. Although the mesh effects are obviously present, the errors are due to predictable

DOI: 10.1002/fld

Table I. Elastic stiffness and damping parameters of five membranes.

Case	1	2	3	4	5
Π	4.0	6.0	7.9	11.0	15.0
EA	5.12e6	1.73e7	4.00e7	1.07e8	2.70e8
λ	64.0	117.6	178.9	291.9	464.6

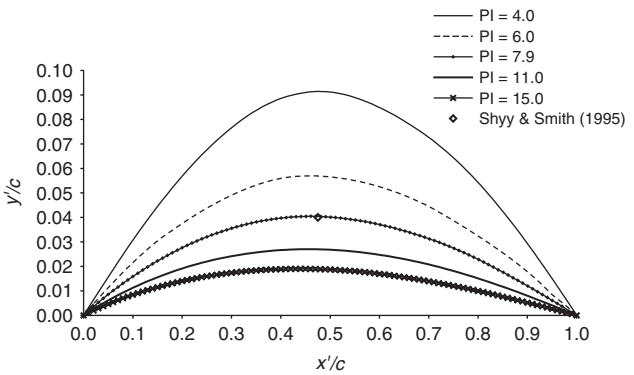

Figure 13. Membrane profiles at non-dimensional time $t=35$ for membranes with varying elastic stiffness. Comparison with Shyy and Smith [8].

effects, and comparison between different membrane properties will still be achievable since the mesh effect will be comparable across all cases using the same mesh and flow at the same Reynolds number.

3.2.2. Membrane elasticity investigation. As presented in Table I, five membranes having different elastic stiffness are modelled. Again the angle of attack is 4° and the Reynolds number is 4×10^3. The computational parameters are those used in the previous test cases.

The membrane profiles at non-dimensional time $t=35$ in local coordinates (see in Figure 7) are shown in Figure 13 (note that the scale in the y'-direction is magnified with respect to that in the x'-direction for clarity). As expected, the lower the elastic stiffness of the membrane, the more pronounced the curved shape that the membrane adopts. The shapes also show an asymmetry since the point of maximum normal displacement (maximum height) is upstream of the chord midpoint. This effect becomes more pronounced as the membrane stiffness is increased. Also plotted on Figure 13 is the point of maximum normal displacement for the same test case with $\Pi=7.9$ presented by Shyy and Smith [8], which shows excellent agreement. Figure 14 shows the maximum normal displacement (maximum height) for each non-dimensional Π value tested. It is clear that an inverse relationship exists between membrane elasticity and height of the equilibrium shape, as expected. The results again agree very well with the data of Shyy and Smith [8].

Considering the aerodynamic forces on the steady membrane shapes, Figure 15 shows the relationship between the maximum normal displacement of the membrane and the drag and lift performance of this shape in each case. The data from Shyy and Smith [8] is again included for comparison, along with an analysis, using the present method, of the flow around a rigid flat

DOI: 10.1002/fld

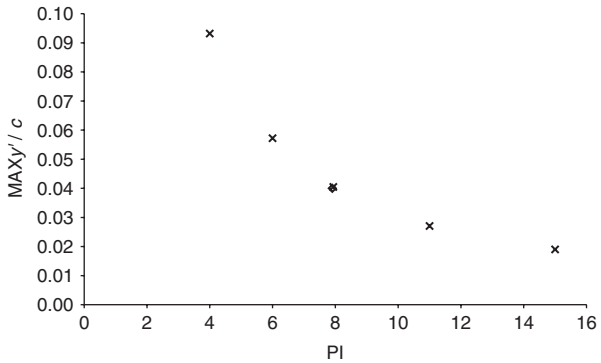

Figure 14. Variation of maximum normal displacement with PI. ×, present study; ◇, Shyy and Smith [8].

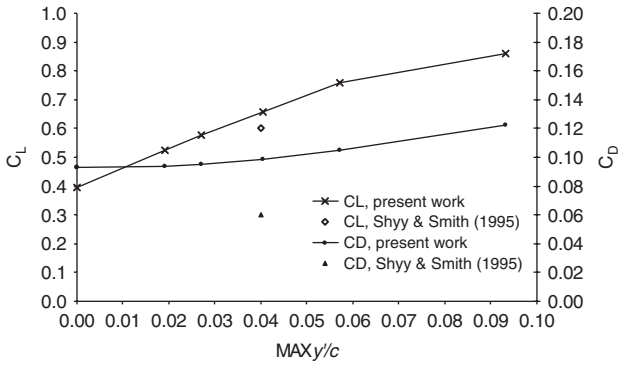

Figure 15. Variation of drag and lift coefficients with non-dimensionalized maximum normal displacement of the membrane shape. Comparison with Shyy and Smith [8].

plate at the same angle of attack and free stream velocity (i.e. corresponding to an infinitely stiff membrane). The data points have been connected with straight lines for clarity. It is clear that for the lower profile membranes, increasing the height of the curved shape (for example, by reducing the elastic stiffness) has the effect of increasing the lift forces on the surface much more quickly than the drag forces. However, as the height of the membrane is increased further, it can be seen that the rate of increase in drag increases, while the rate of increase in lift decreases. This is in keeping with classical aerofoil performance data if we consider the effects of membrane height to be equivalent to those of the angle of attack of an aerofoil. Both lift and drag increase as the angle of attack is increased, and once the boundary layer separates from the aerofoil surface and the region of separated flow grows in size, the rate of increase of lift decreases, while the rate of increase of drag increases.

It is clear from Figure 15 that the present results for lift forces agree much more closely with the data of Shyy and Smith [8] than those for drag. This is in keeping with the observations made earlier concerning the results of the mesh dependency test; since the mesh used here has 100 fluid

DOI: 10.1002/fld

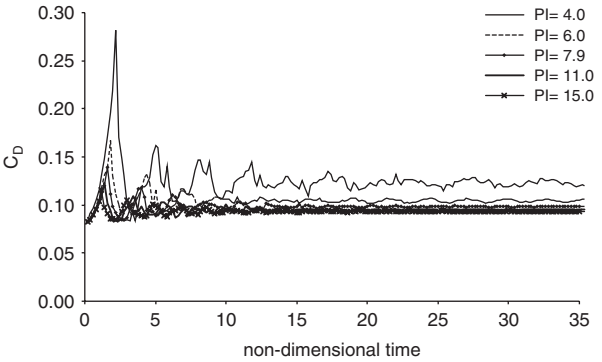

Figure 16. Time history of drag coefficient for membranes with varying elastic stiffness.

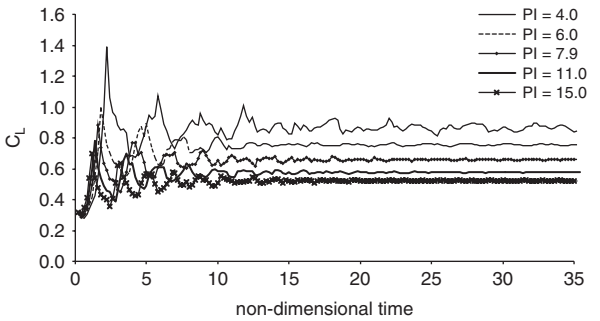

Figure 17. Time history of lift coefficient for membranes with varying elastic stiffness.

elements on the membrane surface, it is to be expected that a discrepancy in overall drag forces will result, while the lift forces will be significantly more accurate.

The time histories of the drag and lift coefficients are presented in Figures 16 and 17, respectively. It can be seen that, the lower the elastic stiffness of the membrane, the higher both the drag and lift forces on the resulting steady form. It can also be seen that the lower the elastic stiffness of the membrane, the longer the membrane takes to adopt its final steady shape. Furthermore, clear oscillations can be observed in both lift and drag in all five cases, and both the time period and the magnitude of these oscillations reduce as the stiffness reduces.

Figures 16 and 17 also show that the oscillations in drag and lift forces become more complex, as the stiffness of the membrane reduces. This suggests that the lower elasticity membranes support more complex superimposed oscillations for longer periods of time than the stiffer membranes; the stiffer membranes appear overall more efficient at damping out vibrations. In fact it can be seen that the membranes in Case 1 and to a lesser extent Case 2 have not yet settled into a stable shape. This will be examined further in the following discussions.

A further point of interest that could offer insight into this behaviour can be seen from considering the motion of the midpoint of the membrane over time in each case. The relative magnitude of the displacements of the midpoint of the membranes over time in local x' and local y' is shown in Figure 18, in which the x' displacement is described as a percentage of the y' displacement at a

DOI: 10.1002/fld

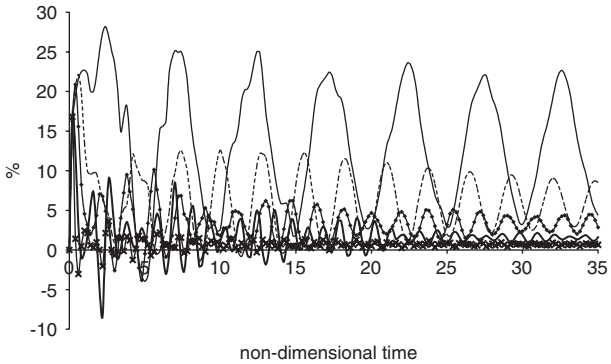

Figure 18. Time history of displacements of the midpoint of the membrane; displacement in local x as a percentage of displacement in local y, for membranes with varying elastic stiffness. Legend as Figure 17.

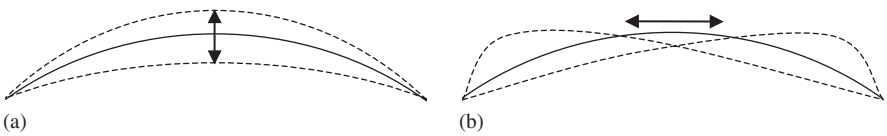

Figure 19. (a) and (b) Mode shapes of vibration.

given time instant. It can be seen that in the most flexible case. Case 1, the membrane oscillations along the chord are larger with respect to the membrane oscillations normal to the chord. The relative magnitude of the x' oscillations decreases as the membrane stiffness increases.

The mode of oscillation of an elastic arch corresponding to a midpoint displacement only in y' is the symmetric extensional mode shown in Figure 19(a). The mode of oscillation of an arch corresponding to a midpoint displacement only in x' is the asymmetrical inextensional mode shown in Figure 19(b). It is therefore likely that the motion of the less stiff membranes is tending towards mode (b), while the stiffer membranes are tending towards mode (a). The less stiff membranes present a greater height to the oncoming flow and therefore experience a greater net pressure force in the local x'-direction, and also create a larger wake which could induce the asymmetrical oscillations. The stiffer membranes present a smaller height and therefore experience a less significant net pressure force in this direction. Furthermore, the asymmetrical mode (b) involves no stretching of the membrane, and therefore the membrane can deform in this mode without inducing internal elastic forces. The symmetrical mode (a) involves elastic stretching of the membrane and therefore also internal damping of its motion, which supports the observation that the more stiff the membrane, the quicker the oscillations decay. For the more flexible membranes, when the membrane height is sufficiently high to observe the asymmetrical mode (b) displacements, the oscillation persists for a much greater period of time since no internal damping is induced.

It can be seen for Case 1 that the membrane does not appear to settle into a steady shape for a considerably longer period of time than all the other tests. The lift and drag coefficients for Case 1 up to non-dimensional time $t=200$ are shown in Figure 20, which shows clear sustained oscillations in the aerodynamic coefficients. Although the oscillations in lift and drag do appear to be slowly reducing in amplitude, it is not clear if the simulation is converging to a stable state or if

DOI: 10.1002/fld

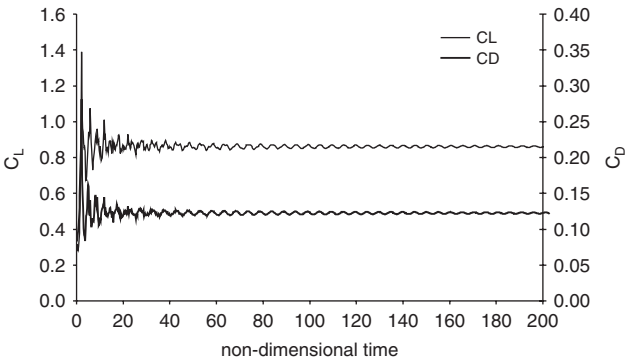

Figure 20. Time history of lift and drag coefficients on membrane Case 1, $\Pi = 4.0$.

a steady oscillation will result. These oscillations could correspond to the oscillations seen in the other test cases as the membrane moves towards its steady shape; however, in Cases 3–5 it is clear that the oscillations in the membrane are eventually damped out by the structure and the fluid after a non-dimensional time period between 35 and 55, and a steady shape results. Alternatively these sustained oscillations could be an indication of a more complex interaction behaviour between the membrane and the flow in this most flexible case. Closer inspection of the position of the midpoint of the Case 1 membrane over time shows that the oscillations in x' and y' are in phase with each other, and also in phase with the oscillations in both drag and lift coefficients.

Case 1 presents the most pronounced membrane profile to the flow as shown in Figure 13, and inspection of the velocity vectors near the trailing edge shows the existence of a pair of vortices here, as shown in Figure 21. Inspection of the wake over time shows that the vortices do not appear to be shed into the flow, but remain attached to the trailing edge of the membrane. Hence, to investigate the oscillations in the aerodynamic coefficients further, an average membrane shape (the shape found at a time instant corresponding to the mean midpoint displacements over the period $t = 120$ to 140) is analysed as a rigid structure, to see whether the trailing vortices are stable or are shed into the flow in the equivalent case with no fluid–structure interaction.

As shown in Figure 22, both the lift and drag coefficients for this rigid curved shape demonstrate a small oscillation in value. After running the simulation to a non-dimensional time $t = 25$, no discernible decay in the oscillations in drag and lift was present, i.e. the oscillations are stable. To verify that this is a flow-induced effect, rather than a numerical error, the flow about the same rigid shape was analysed at a much lower velocity giving a Reynolds number of 40. The evolution of the drag and lift coefficients in this case is shown in Figure 23, respectively. Since no oscillation is found here, this suggests that the oscillation shown in Figure 22 is due to slight wobbling of the vortices in the wake.

In both the flexible and rigid cases, shedding of vortices into the wake does not occur; the vortices remain attached and the observed oscillation is due to their interaction. On comparison, both cases demonstrate oscillations about the same mean value for both lift and drag coefficients; 0.860 and 0.123, respectively. However, while the flexible case oscillation in drag is $\pm 0.8\%$ and lift $\pm 0.5\%$, in the rigid case the corresponding magnitudes are ± 0.003 and $\pm 0.02\%$, respectively. Furthermore, the flexible case coefficients both oscillate at a non-dimensional frequency of 0.2 Hz, while in the rigid case the non-dimensional frequency is 1.9 Hz.

DOI: 10.1002/fld

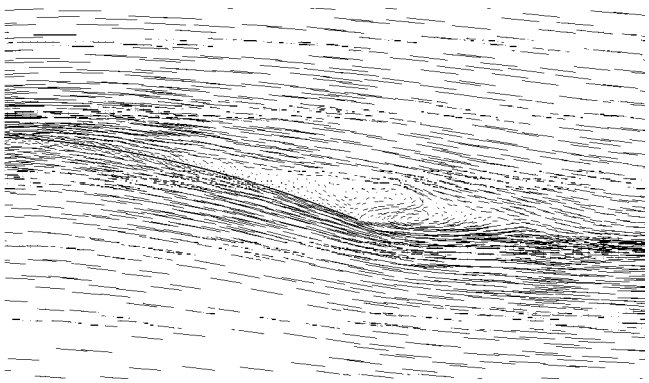

Figure 21. Velocity vector plot for Case 1, $\Pi = 4$, at non-dimensional $t = 35$ showing attached vortices at the trailing edge.

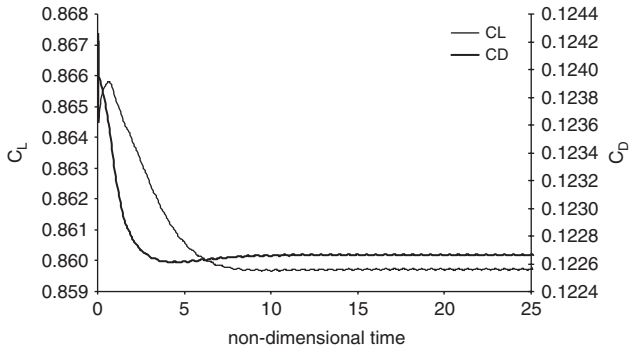

Figure 22. Time history of lift and drag coefficients for rigid shape corresponding to mean Case 1 profile.

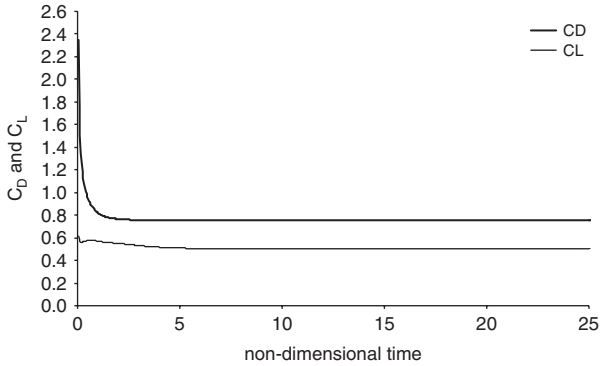

Figure 23. Time history of lift and drag coefficients for rigid shape corresponding to mean Case 1 profile, $Re = 40$.

DOI: 10.1002/fld

In the flexible case the magnitude of oscillation in drag and lift forces is considerably larger than that observed in the rigid case and the frequency of oscillation is an order of magnitude lower, demonstrating that the flexible nature of the membrane is causing a significant interactive effect to occur between the membrane shape and the flow around it, in particular in the wake. The relatively small unsteadiness observed in the rigid case is greatly magnified in the coupled flexible system.

The computational time required for the calculations varies considerably from case to case, and during each simulation, since it depends on the number of iterations required to converge both the fluid and mesh solutions. For the fluid, the number of iterations to cause convergence will depend, for example, on the rate of change of the flow field from one timestep to the next. For the mesh, larger boundary motions will require more iterations to 'smooth' the interior mesh nodes. It is therefore not possible to generalize the increased computation required in a coupled fluid–structure simulation compared with the one in which the structure remains fixed. However, as a comparison, we can consider the test cases of the least stiff membrane, analysed once with a flexible shape and once with a rigid shape as previously described, which use the same mesh and the same timestep. Averaging the computational time over the simulations, which were carried out on a desktop pc, the rigid case requires 1.84×10^4 s real time to analyse 1 non-dimensional second, and the flexible case requires 2.08×10^4 s, an increase of 13%.

4. CONCLUSION

A method has been presented which is designed for application to fluid–flexible structure interaction problems. Unstructured triangular meshes are used with the collocated finite volume method to discretize the Navier–Stokes equations, taking into account the effects of grid non-orthogonality, and the power law interpolation scheme is used for stability. The pressure solution is found using the SIMPLE algorithm. A new membrane elasticity model has been presented for the discretization of the membrane structure, which allows for global and local elastic effects and includes damping.

The method has successfully been applied to the investigation of the behaviour of two-dimensional two-pinned membrane airfoils of varying stiffness, in an oncoming flow of Reynolds number 4000. It is clear that pressure difference across the membrane is the primary lift generation mechanism, while viscous stresses dominate the drag effect. This highlights the need for a fully viscous flow solver to model these systems in order to accurately predict the drag forces. The importance of accurately modelling the velocity gradient in the vicinity of the structure is also demonstrated. Good agreement with published data for the stable membrane shape and lift forces is achieved, while errors in drag prediction are shown to be highly dependent on mesh spacing in the boundary layer normal to the membrane surface.

As expected, the stiffer the membrane, the lower the steady profile shape adopted. Considering the unsteady behaviour towards a steady equilibrium shape, the stiffer the membrane, the quicker the shape will be adopted, the more the membrane oscillations will be orientated in the local y-direction and the higher the frequency of these oscillations. The lower stiffness membranes exhibit sustained oscillations in shape, with a more significant displacement component along the chord direction indicating a tendency towards an asymmetrical inextensional vibration mode.

The method has successfully shed light on situations where a stable shape is not adopted, and can be used to predict membrane oscillations, including unsteady interactions with the wake, and to study in detail the modes of vibration.

DOI: 10.1002/fld

REFERENCES

1. van Loon R, Anderson PD, van de Vosse FN. A fluid–structure interaction method with solid-rigid contact for heart valve dynamics. *Journal of Computational Physics* 2006; **217**:806–823. DOI: 10.1016/j.jcp.2006.01.032.
2. Shyy W, Francois M, Udaykumar HS, N'dri N, Tran-Son-Tay R. Moving boundaries in micro-scale biofluid dynamics. *Applied Mechanics Reviews* 2001; **54**:405–453.
3. Tezduyar T, Osawa Y. Fluid–structure interactions of a parachute crossing the far wake of an aircraft. *Computer Methods in Applied Mechanics and Engineering* 2001; **191**:717–726.
4. Mestreau E, Löhner R. Airbag simulation using fluid–structure coupling. *Proceedings of the 34th Aerospace Sciences Meeting and Exhibit*, 15–18 January 1996, Reno, NV, U.S.A., AIAA-96-0798.
5. Schoop H, Bessert N. Instationary aeroelastic computation of yacht sails. *International Journal for Numerical Methods in Engineering* 2001; **52**:787–803.
6. Lian Y, Shyy W. Three-dimensional fluid–structure interactions of a membrane wing for micro air vehicle applications. *Proceedings of the 44th AIAA/ASME/ASCH/AHS/ASC Structures, Structural Dynamics and Materials Conference*, 7–10 April 2003, Norfolk, VA, U.S.A., AIAA 2003-1726.
7. Glück M, Breuer M, Durst F, Halfmann A, Rank E. Computation of fluid–structure interaction on lightweight structures. *Journal of Wind Engineering and Industrial Aerodynamics* 2001; **89**:1351–1368.
8. Shyy W, Smith R. Computation of laminar flow and flexible structure interaction. In *Computational Fluid Dynamics Review*, Hafez M, Oshima K (eds). Wiley: New York, 1995.
9. Peskin CS, McQueen DM. A general method for the computer simulation of biological systems interacting with fluids. *Proceedings of SEB Symposium on Biological Fluid Dynamics*, Leeds, England, 5–8 July 1994.
10. Lian Y, Steen J, Trygg-Wilander M, Shyy W. Low Reynolds number turbulent flows around a dynamically shaped airfoil. *Computers and Fluids* 2003; **32**:287–303.
11. Xu Z, Accorsi M. Finite element mesh update methods for fluid–structure interaction simulations. *Finite Elements in Analysis and Design* 2004; **40**:1259–1269.
12. Robinson BA, Batina JT, Yang HTY. Aeroelastic analysis of wings using the Euler equations with a deforming mesh. *Journal of Aircraft* 1991; **28**:781–788.
13. Degand C, Farhat C. A three-dimensional torsional spring analogy method for unstructured dynamic meshes. *Computers and Structures* 2002; **80**:305–316.
14. Bunge U, Rung T, Thiele F. A two-dimensional sail in turbulent flow. *Proceedings of the 1st International Conference on Fluid Structure Interaction*, Halkidiki, Greece, 2001.
15. Jackson PS, Christie GW. Numerical analysis of three-dimensional elastic membrane wings. *AIAA Journal* 1987; **25**:676–682.
16. Schoop H, Bessert N, Taenzer L. On the elastic membrane in a potential flow. *International Journal for Numerical Methods in Engineering* 1998; **41**:271–291.
17. Jackson PS, Fiddes SP. Two-dimensional viscous flow past flexible sail sections close to ideal incidence. *The Aeronautical Journal* 1995; **99**:217–225.
18. Cyr S, Newman BG. Flow past two-dimensional membrane aerofoils with rear separation. *Journal of Wind Engineering and Industrial Aerodynamics* 1996; **63**:1–16.
19. Smith R, Shyy W. Computation of aerodynamic coefficients for a flexible membrane airfoil in turbulent flow: a comparison with classical theory. *Physics of Fluids* 1996; **8**:3346–3353.
20. Newman BG. Aerodynamic theory for membranes and sails. *Progress in Aerospace Sciences* 1987; **24**:1–27.
21. 'Triangle', Jonathan Schewuck, http://www.cs.cmu.edu/∼quake/triangle.html.
22. Rhie CM, Chow WL. Numerical study of the turbulent flow past an airfoil with trailing edge separation. *AIAA Journal* 1983; **21**:1525–1532.
23. Muzaferija S. Adaptive finite volume method for flow predictions using unstructured meshes and multigrid approach. *Ph.D. Thesis*, University of London, London, 1995.
24. Thomas PD, Lombard CK. Geometric conservation law and its application to flow computations on moving grids. *AIAA Journal* 1979; **17**:1030–1037.
25. Lesoinne M, Farhat C. Geometric conservation laws for flow problems with moving boundaries and deformable meshes, and their impact on aeroelastic computations. *Computer Methods in Applied Mechanics and Engineering* 1996; **134**:71–90.
26. Patankar SV, Spalding DB. A calculation procedure for heat, mass and momentum transfer in three-dimensional parabolic flows. *International Journal of Heat and Mass Transfer* 1972; **15**:1787–1806.
27. Hudson JD, Dennis SCR. The flow of a viscous incompressible fluid past a normal flat plate at low and intermediate Reynolds numbers: the wake. *Journal of Fluid Mechanics* 1985; **160**:369–383.

28. Dennis SCR, Quiang W, Coutanceau M, Launay J-L. Viscous flow normal to a flat plate at moderate Reynolds numbers. *Journal of Fluid Mechanics* 1993; **248**:605–635.
29. Archivos A, Leal LG, Snowden DD, Pan F. Further experiments on steady separated flows past bluff objects. *Journal of Fluid Mechanics* 1968; **34**:25–48.
30. Smith FT. On large-scale eddy closure. *Journal of Mathematical and Physical Sciences* 1985; **19**:1–80.
31. Ingham DB, Tang T, Morton BR. Steady two-dimensional flow through a row of normal flat plates. *Journal of Fluid Mechanics* 1990; **210**:281–302.

DOI: 10.1002/fld